# Fiber Bragg Gratings for Temperature Measurements Under Thermal Gradients: Comparison Between Two Different Lengths

Francesca De Tommasi, *Student Member, IEEE*, Livio D'Alvia, *Member, IEEE*, Carlo Massaroni, *Senior Member, IEEE*, Daniela Lo Presti, *Member, IEEE*, Massimiliano Carassiti, Zaccaria Del Prete, *Member, IEEE*, Emiliano Schena, *Senior Member, IEEE*, and Eduardo Palermo, *Member, IEEE*

***Abstract*— In recent decades, fiber Bragg grating (FBG) sensors found widespread acceptance in several biomedical applications thanks to their indisputable advantages. Thermal ablation treatments (TATs) account for one of the fields where FBGs have gained large applicability for temperature measurements. The sensing element length can affect the accuracy of the FBG measurement in this application. A longer length provides a more prominent peak in the FBG reflected spectrum, resulting in a higher signal-to-noise ratio (SNR). A shorter FBG length implies a lower SNR but offers the benefits of better spatial resolution. Therefore, the choice of an adequate length can be crucial to minimize measurement errors, but the literature lacks exhaustive investigations on this parameter. The aim of our study is to supply additional knowledge about the effect of two different FBG lengths on temperature estimation in the presence of linear thermal gradients and with gradients mimicking the condition caused by TATs. In both cases, we compared the output of a 10-mm FBG with those of four FBGs 1 mm long, using a thermal camera as a reference instrument. Results suggest the better suitability of shorter sensors to retrieve thermal gradient information along their position instead of the longer FBG, which could lead to unacceptable measurement errors during TATs.**

***Index Terms*— Fiber Bragg grating (FBG) sensors, temperature measurements, thermal ablation treatments (TATs), thermal gradients.**

## I. Introduction

SINCE their discovery, the exploitation of fiber Bragg grating (FBG) sensors burst in a variety of fields and are nowadays widely leveraged in medical and biomedical applications [1], [2], [3], [4]. Their popularity is driven by a number of distinctive features such as their biological compatibility, nontoxicity, reduced size, inherent safety, electromagnetic disturbance immunity, and capacity for multiplexing [5].

Among the domains of applicability in medicine, thermal ablation treatments (TATs) are one of the leading areas of FBGs for temperature measurements purposes [6], [7], [8], [9], [10], [11]. Hyperthermia-based TATs work to induce a rise in temperature up to a cytotoxic level (>50 °C) with the goal of permanently damaging tumor masses [12]. In general, they are performed by means of a needlelike applicator located under imaging guidance in the malignant area, responsible for energy delivery (i.e., microwave, radio frequency, or light according to the source employed) [13]. The energy-tissue interaction results in the temperature increase inside the tissue. The extent of the injured volume depends on temperature values achieved, and the time over which they persist, as suggested by the thermal damage models broadly deployed in this field (i.e., Arrhenius's law and CEM43) [14]. Despite the ongoing widespread deployment of TATs, forecasting their effects still remains a huge hurdle due to the complex mechanisms of interaction and the different boundary conditions among patients (e.g., tumor size, position, and presence of large blood vessel in the proximity of malignant cells) [15], [16], [17]. Thus, tracking temperature during the procedure can be instrumental in monitoring the damaged tissue accurately and safeguarding surrounding healthy anatomical structures, thus preventing careless and ineffective treatments. Scientific research studies suggest a temperature accuracy of 1 °C–2 °C for monitoring TATs [18]. In this context, FBGs emerge as a viable technique for monitoring temperature compared with both contact (e.g., thermocouples or thermistors) and noncontact-based (e.g., computed tomography or magnetic resonance) [19]. Indeed, electrical transducers suffer from the main impediment of single-point measurements, limiting the ability to accurately reconstruct the heat map of the tissue surrounding the applicator. This anatomical portion experiences a considerable thermal gradient (around 10 °C/cm–20 °C/cm and up to 50 °C/cm in the proximity of the applicator tip) [20], thus gaining information on the temperature reached at one point is insufficient to retrieve the temperature distribution of the entire tissue treated. Conversely, diagnostic imaging techniques can reconstruct the thermal map with high spatial

Manuscript received 28 January 2023; revised 3 April 2023; accepted 26 April 2023. Date of publication 15 May 2023; date of current version 21 June 2023. The Associate Editor coordinating the review process was Dr. Anoop Chandrika Sreekantan. *(Corresponding author: Carlo Massaroni.)*

Francesca De Tommasi, Carlo Massaroni, Daniela Lo Presti, and Emiliano Schena are with the Unit of Measurements and Biomedical Instrumentation, Faculty of Engineering, Università Campus Bio-Medico di Roma, 00128 Rome, Italy (e-mail: c.massaroni@unicampus.it).

Livio D'Alvia, Zaccaria Del Prete, and Eduardo Palermo are with the Department of Mechanical and Aerospace Engineering, "Sapienza" University of Rome, 00184 Rome, Italy.

Massimiliano Carassiti is with the Fondazione Policlinico Universitario Campus Bio-Medico, 00128 Roma, Italy, and also with the Research Unit of Anesthesia, Intemsive Care and Pain Management, Department of Medicine and Surgery, Università Campus Bio-Medico di Roma, 00128 Roma, Italy.

Digital Object Identifier 10.1109/TIM.2023.3276511

resolution but lack adequate accuracy and dynamic response and are expensive. Although their invasive nature, FBGs overcome the raised limitations. Among their aforementioned advantages, the multiplexing capability provides for multipoint measurements and gathering temperature maps with high spatial resolution and accuracy.

In general, FBGs employed during TATs can have different sensing lengths, usually ranging between 1 and 10 mm [21], [22], [23], [24]. However, the FBG length should be carefully selected as it influences the FBGs' spectral response, and thus the temperature estimation [25]. FBGs with a longer length are marked by a more prominent peak in the reflected spectrum, which results in a higher signal-to-noise ratio (SNR). On the other hand, shorter length FBGs imply a broadband spectrum and weaker peak, hence a lower SNR, while affording the advantages of higher spatial resolution. For this reason, choosing a suitable length capable of ensuring adequate spatial resolution and accuracy is of paramount importance to avoid unacceptable measurement errors, resulting in misleading assumptions regarding the TAT outcome. In the literature, studies addressing this issue in TATs are very limited [26], [27]. In [26], the influence of FBGs lengths on temperature measurements was assessed in laboratory tests and ex vivo liver ablation. However, in the first case, the reference temperature was monitored by means of only two thermocouples placed at the extremities of the longest FBG, disregarding a temperature analysis along the entire sensitive length. Instead, for the second setting, the output of FBGs with shorter and higher lengths was compared with each other without any reference instrument. Differently, in the study carried out by Gassino et al. [27], the different length FBGs response was investigated by simulating laser ablation (LA) using a linear resistor and an agar disk and, therefore, farther from the real conditions.

In this study, we provide additional insights about the influence of FBG length on temperature estimation in the presence of different thermal gradients. We performed bench tests and ex vivo LA to mimic as much as possible the real clinical scenario. In both cases, we employed FBGs with two different lengths (i.e., 10 and 1 mm) to compare their output when subjected to relevant thermal gradients. For both scenarios, a thermal camera was used as a reference instrument to determine the temperature values experienced by the FBGs along their whole sensitive length. We demonstrated that using short FBGs (i.e., 1 mm in length) allows for better results than longer FBGs (i.e., 10 mm in length) in case of relevant thermal gradient; thus, their choice is advisable in TATs.

## II. FBGs: Theoretical Fundamentals and Metrological Characterization

### A. FBG Working Principle and Spectrum Characteristics

An FBG is an optical sensor inscribed inside the core of an optical fiber, acting as a notch filter. To manufacture the sensor, a variable UV light pattern acts on the fiber core, thus causing a permanent periodic perturbation of the effective refractive index ($n_{\text{eff}}$). Thus, light crossing the optical fiber core is partially reflected when it encounters the grating.

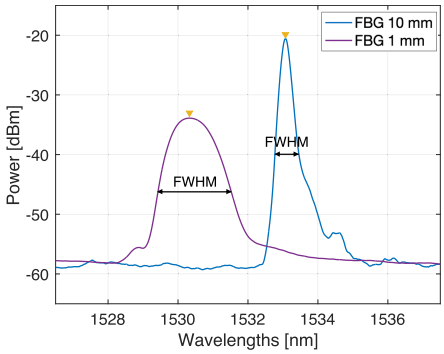


Fig. 1. Example of reflected spectra belonging to FBGs of 10 and 1 mm in length.

The back-reflected small portion of wavelengths is centered around the so-called Bragg wavelength (i.e., $\lambda_B$), satisfying the following relationship [28]:

$$\lambda_B = 2 \cdot n_{\text{eff}} \cdot \Lambda \tag{1}$$

where $\Lambda$ denotes the spatial grating period. Both $n_{\text{eff}}$ and $\Lambda$ are influenced by strain ($\epsilon$) or temperature variation ($\Delta T$) acting on the grating. So, when the fiber is subjected to perturbation in terms of $\epsilon$ and/or $\Delta T$, a shift in $\lambda_B$ occurs as attested by the equation below [29]

$$\frac{\Delta\lambda_B}{\lambda_B} = (1-\rho_\alpha)\cdot\epsilon + (\alpha+\xi)\cdot\Delta T \tag{2}$$

where $(1-\rho_\alpha)\cdot\epsilon$ addresses the strain effect and $(\alpha+\xi)\cdot\Delta T$ the temperature one on the optical fiber. Specifically, $\rho_\alpha$, $\alpha$, and $\xi$ refer to the photoelastic, thermal expansion, and thermo-optical coefficients. FBGs are used as temperature sensors only during TATs, considering negligible strain contributions. So, the previous equation can be simplified as follows:

$$\Delta\lambda_B = S_T \cdot \Delta T. \tag{3}$$

The term $S_T$ represents the thermal sensitivity value.

Since temperature measurements through FBG sensors rely on the tracking of wavelength shift of the grating peak, the analysis of their spectral response and related characteristics is an important factor as they are affected by the grating length and also change in the presence of thermal gradients [25], [30]. The characteristics of the reflected spectrum impacted by these two parameters are the reflectivity and the bandwidth. The first refers to the light percentage reflected in correspondence of $\lambda_B$ [25]. The reflectivity value rises with the increase in grating length, resulting in a higher SNR in peak detection. Whereas, the bandwidth represents the spectral width of the reflected spectrum measured as the full width at half maximum (FWHM). This parameter is measured as the distance between the two points at which the curve achieves half of its highest value (as evidenced in Fig. 1), and decreases with the increase of FBG length [25]. Since the FBG output depends on the temperature applied to its sensing part, some studies have investigated how the temperature gradient influences the FWHM. Experiments showed that the FWHM values of uniform and chirped FBGs increase with the thermal gradient [26], [31], [32].

Basically, unlike sensors with longer lengths, those with shorter ones are characterized by a reflected spectrum with a

TABLE I
FBGs Characteristics

| | $\lambda_B$ [nm] | Length [mm] | Reflectivity value [%] |
|---|---|---|---|
| FBG10 | 1533 | 10 | 94.37 |
| FBG1 | 1510 | 1 | 52.57 |
| FBG2 | 1520 | 1 | 52.35 |
| FBG3 | 1530 | 1 | 51.58 |
| FBG4 | 1540 | 1 | 52.35 |

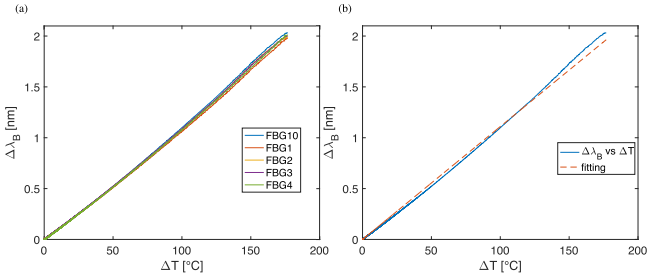


Fig. 2. (a) Experimental data ($\Delta\lambda_B$ versus $\Delta T$) for each FBG denoted with different colors (i.e., blue for FBG10, orange for FBG1, yellow for FBG2, violet for FBG3, and green for FBG4) obtained experimentally after the characterization process. (b) Example of experimental data (blue line) collected during the characterization of one FBG (i.e., FBG10) and the best fitting line (orange dashed line).

less prominent peak, a higher FWHM, and a lower reflectivity value (Fig. 1 highlighted the difference between them). In the case of TAT application, the presence of very high thermal gradients in a limited tissue portion would ideally require punctual temperature measurements at multiple locations around the applicator. However, an increase in spatial resolution leads to a noise increment in the signal. Therefore, proper tradeoffs need to be found.

In this study, the spectral response of each FBG in the presence of different thermal gradients was assessed in terms of $\lambda_B$ changes and FWHM.

### B. Metrological Characterization

To assess the influence of FBG length on temperature estimation, we used two single-mode optical fibers acrylate coated (i.e., Technica Optical Components, Atlanta, GA, USA) for both bench tests and ex vivo LA. The first fiber embedded a single 10 mm long uniform FBG (model number T10 [33], hereafter FBG10), while the second one was an array of four uniform FBGs having a length of 1 mm each and spaced 2 mm edge-to-edge (model number T100 [34], hereafter FBG1–FBG4) realized by means of a UV laser phase mask technique. Table I reports $\lambda_B$ values, length, and reflectivity values for each FBG.

Before starting experiments, each FBG was characterized to assess its thermal sensitivity value ($S_T$). A laboratory oven (i.e., PN120 Carbolite) was employed to expose the two optical fibers to a range of temperatures spanning from 23 °C to 200 °C. A $K$-type thermocouple (Testo SE & Company KGaA, Lenzkirch, Germany) allowed for collecting the reference temperatures (i.e., the ones imposed in the oven) through a sampling rate of 0.1 Hz. At the same time, the FBGs' output was recorded via an optical interrogator (si255 Micron Optics Inc., USA) at a fixed frequency of 1 Hz. An ad hoc algorithm developed in the MATLAB environment was implemented to obtain the calibration curve ($\Delta\lambda_B$ versus $\Delta T$) for each FBG [as evidenced in Fig. 2(a)]. Thus, it was possible to retrieve the $S_T$ values as the angular coefficients of the lines closely fitting our experimental data [as shown as an example in Fig. 2(b)], and the correlation coefficient (i.e., $R^2$) was used to assess the interpolation goodness. Table II reports the results obtained in terms of both $S_T$ and $R^2$. As evidenced, $S_T$ values are equal to 11 pm $\cdot^\circ$ C$^{-1}$ and close to those reported by the manufacturer.

TABLE II
Thermal Sensitivity Values and Correlation Coefficients

| FBG | $S_T$ [pm $\cdot$ °C$^{-1}$] | $R^2$ |
|---|---|---|
| FBG10 | 11 | 0.998 |
| FBG1 | 11 | 0.999 |
| FBG2 | 11 | 0.998 |
| FBG3 | 11 | 0.999 |
| FBG4 | 11 | 0.998 |

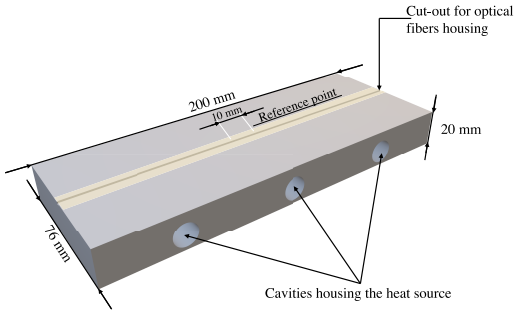


Fig. 3. Aluminum bar manufactured for the arrangement of optical fibers and heat and cold sources.

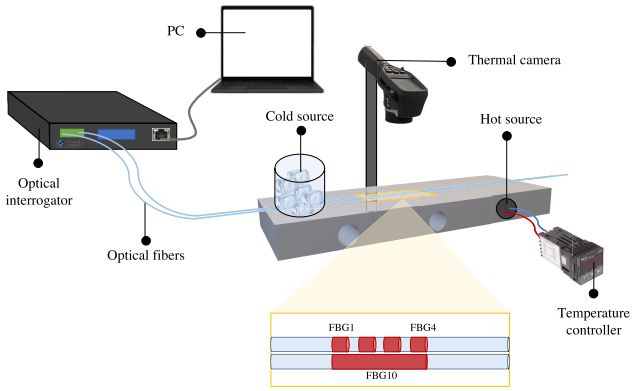


Fig. 4. Experimental setup employed during bench tests: the aluminum bar, two optical fibers (one hosting the FBG10 and the other housing FBG1–FBG4), two heat sources (an ice box on the left side and a cartridge heater on the right one of the bar), a controller, an optical interrogator, a PC, and a thermal camera as a reference instrument.

## III. Influence of Two Bragg Grating Lengths on Temperature Estimation Under Controlled Conditions

### A. Experimental Setup of Bench Tests

In the first step, we performed two bench tests under laboratory-controlled conditions. The two optical fibers were arranged in the middle of an ad hoc manufactured aluminum bar. The proposed bar is rectangular in shape (200 × 76 × 20 mm) with a central cut-out of 2 mm in width and

1 mm in depth for accommodating the fibers. This solution avoided using any additional material to fix the fibers on the bar. Lateral cavities were designed to house a cylindrical heating resistor used as the heat source during bench tests (as evidenced in Fig. 3). In addition, two reference points were realized on the upper surface of the bar to facilitate the positioning of the FBGs during the experiments at a distance of 10 mm from each other (Fig. 3).

During tests, a linear thermal gradient was imposed along the bar using a hot source and cold source placed at the two extremities of the aluminum bar, see Fig. 4. A beaker containing ice was used as a cold source at a constant temperature of about 0 °C and placed on the top surface at one extremity of the bar. A cartridge heater (RS-8606766, RS, Corby, U.K.) was placed on the opposite side (exploiting one of the lateral cavities). To raise the resistor to the desired temperature, we used a PID temperature controller (N6500Z210000, RS, Corby, U.K.), which allowed us to set the desired temperature controlled by a type-$K$ thermocouple. In our cases, the set-point temperature was imposed equal to 70 °C and 90 °C for the first and second tests, respectively.

To compare the $\Delta T$ values estimated by FBGs of different lengths, the four FBGs of 1 mm (i.e., FBG1–FBG4) were placed parallel to the 10-mm FBG (i.e., FBG10) and in such a way that they covered its sensitive length (as shown in Fig. 4). FBGs' output was collected by means of an optical interrogator (si255 Micron Optics Inc., USA) at a sampling rate of 1 kHz. A thermal camera (FLIR E50, FLIR Systems s.r.l.) was used as a reference instrument to measure the temperature. This camera has an IR resolution of 240 × 180 pixels, a spatial resolution of 1.82 mrad, and an accuracy equal to ±2% of the reading value or ±2 °C [35]. The bar was covered with matte black to avoid unintentional interferences or reflections during thermal camera measurements. Sensor placements were guided by two thermally reflective reference points spaced 10 mm apart and made on the top surface of the bar (as evidenced in Fig. 3). Thermographic images were acquired setting an $\epsilon$ equal to 0.99 and at different time instants in the two trials during the experiments (i.e., a total of four different instants of time before hot and cold sources activation, around 3 min after their placement, and the remaining two about every 30 s) and synchronization with FBGs acquisition was carried out using a stopwatch. Fig. 4 shows the overall experimental setup employed during the tests.

### B. Data Analysis

For the sake of comparing the data obtained by the thermal camera and those collected from the FBGs, in the first step, we post-processed the acquired images to extract only the information of our interest (i.e., temperatures of the image area corresponding to FBG positioning, $x = 10$ mm and $y = 2$ mm, hereafter called ROI). For this purpose, each acquired thermographic image was imported into the FLIR TOOLS software to extract temperature values of every pixel, thus obtaining a temperature matrix of 240 × 180. After, in the MATLAB environment, we analyzed each matrix to retrieve only temperatures related to the ROI. This selection provided a temperature matrix, smaller in size than the previous one,

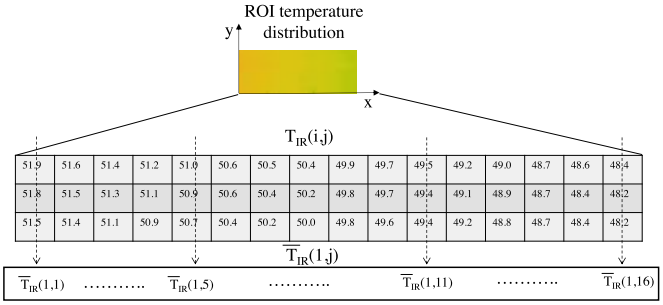


Fig. 5. As an example, the calculation of $\overline{T}_{\mathrm{IR}}(1, j)$ from $T_{\mathrm{IR}}(i, j)$ matrix extracted from the ROI.

$T_{\mathrm{IR}}(i, j)$ where $i$ and $j$ represent the pixels along $y$ and $x$ of the ROI, respectively. From $T_{\mathrm{IR}}(i, j)$, it was possible to display the ROI temperature map, thereby knowing the temperature distribution for each instant.

To visualize the thermal gradient establishing in the ROI at different times, we calculated the mean temperature trend in the ROI from $T_{\mathrm{IR}}(i, j)$ matrix as evidenced in Fig. 5 and expressed in the equation below:

$$\overline{T}_{\mathrm{IR}}(1, j) = \frac{1}{M} \sum_{i=1}^{M} T_{\mathrm{IR}}(i, j) \tag{4}$$

where $M$ represents the number of rows of $T_{\mathrm{IR}}(i, j)$ matrix. Also, we estimated the related standard deviation as follows:

$$\sigma(1, j) = \sqrt{\frac{1}{M-1} \sum_{i=1}^{M} (T_{\mathrm{IR}}(i, j) - \overline{T}_{\mathrm{IR}}(1, j))^2}. \tag{5}$$

Since the FBGs provided temperature variations while thermal camera absolute temperature values, further analysis was needed to compare the output of the two measurement systems. Therefore, for each image acquired, $T_{\mathrm{IR}}(i, j)$ were subtracted from the average values of the image acquired at room temperature in the ROI [i.e., $T_{\mathrm{IR,room}}(i, j)$]. Then, we calculated the mean $\Delta T_{\mathrm{IR}}(i, j)$ trend ($\overline{\Delta T}_{\mathrm{IR}}(1, j)$), according to the following equations:

$$\Delta T_{\mathrm{IR}}(i, j) = T_{\mathrm{IR}}(i, j) - T_{\mathrm{IR,room}}(i, j) \tag{6}$$

$$\overline{\Delta T}_{\mathrm{IR}}(1, j) = \frac{1}{M} \sum_{i=1}^{M} \Delta T_{\mathrm{IR}}(i, j). \tag{7}$$

In addition, the spectra reflected from 10 mm and 1 mm FBG, collected at the same instants of IR image acquisition, were analyzed in terms of $\lambda_B$ values and FWHM of the spectrum. Since changes in $\lambda_B$ and FWHM occur in response to variations in temperature and thermal gradient applied, respectively, we proposed the analysis described below. In the first case, the $\lambda_B$ values were associated with the mean temperature value (i.e., $\overline{T}_{\mathrm{IR}}$) of the ROI estimated by the thermal camera, for each instance as follows:

$$\overline{T}_{\mathrm{IR}} = \sum_{j=1}^{N} \frac{\overline{T}_{\mathrm{IR}}(1, j)}{N} \tag{8}$$

where $N$ represents the number of columns of $\overline{T}_{\mathrm{IR}}(1, j)$. In the second case, the extracted FWHM values were associated with the thermal gradient (i.e., $\mathrm{TG_{IR}}$) retrieved from the IR images calculated as the difference between the maximum and

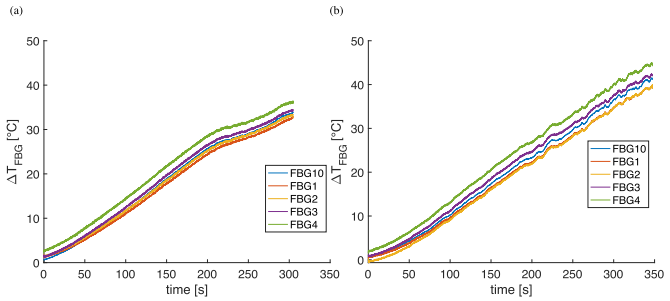


Fig. 6. $\Delta T_{FBG}$ recorded by the FBGs for the entire acquisition time during (a) first bench test and (b) second bench test.

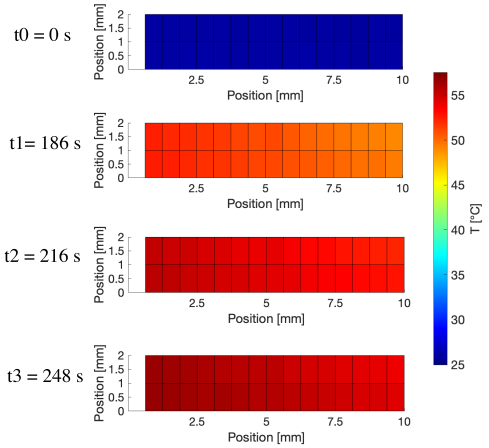


Fig. 7. ROI temperature maps reconstructed from the IR images at specific times (t0-environmental temperature in the absence of hot and cold sources, t1–t3 recorded 186, 216, and 248 s after the positioning of the external hot and cold sources) in the first bench tests.

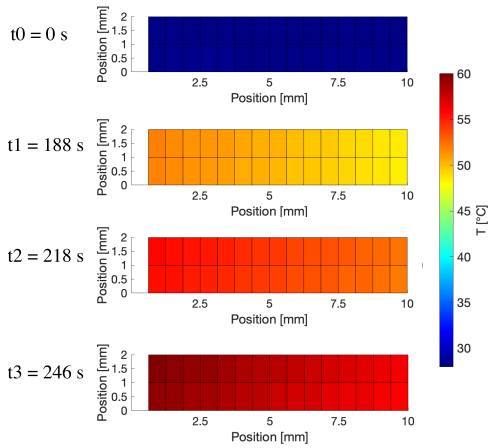


Fig. 8. ROI temperature maps reconstructed from the IR images at specific times (t0-environmental temperature in the absence of hot and cold sources, t1–t3 recorded 188, 218, and 246 s after the positioning of the external hot and cold sources) in the second bench tests.

minimum temperature reached in the ROI, as defined in the following equation:

$$TG_{IR} = \max(T_{IR}(i, j)) - \min(T_{IR}(i, j)). \quad (9)$$

### C. Results

Fig. 6(a) and (b) reports temperature increases estimated by the FBGs (i.e., $\Delta T_{FBG}$) expressed as a function of time acquired for the first and second bench tests. For both tests, the highest temperature values were recorded by the FBG4 of 1 mm in length, which was the closest to the heat source (as evidenced in Fig. 3). The other 1-mm-long FBGs (FBG1–FBG3) experienced lower $\Delta T_{FBG}$ as they were further from the cartridge heater. In both trials, $\Delta T_{FBG}$ values recorded by the 10-mm-long FBG were comparable to the average of the ones experienced by the 1-mm FBGs. In the first bench test, the maximum $\Delta T_{FBG}$ value at the end of the experiment was equal to 36 °C for a set-point temperature imposed to 70 °C. Otherwise, in the second test, the maximum $\Delta T_{FBG}$ at the end was about 44 °C for a maximum temperature set on the controller of 90 °C.

Figs. 7 and 8 show the ROI temperature maps reconstructed from the IR images' temperature values for the first and second tests, respectively, at each instant of time. Specifically, temperature maps denoted with t0 refer to the temperature values extracted from the IR images acquired at room temperature before starting the experiment. The maps titled t1–t3 refer to the images acquired at 186, 216, and 248 s for the first test and 188, 218, and 246 s for the second test after the positioning of the external and cold sources. t1–t3 maps exhibited an intensification toward red due to the temperature increment during the experiment experienced by the whole ROI. The maximum temperature for the first bench test was around 55 °C. Instead, for the second one, the maximum value recorded at t3 was around 60 °C. However, maps did not evidence a relevant thermal gradient in both experiments.

To better visualize the thermal gradient, Fig. 9(a) and (b) shows the mean temperature trend ($\overline{T}_{IR}(1, j)$) and the related standard deviation ($\sigma(1, j)$) recorded in t0–t3 for the first and the second bench tests, respectively. Compared with the average temperature trend extracted from the IR image at room temperature (t0), the other mean trends (see t1–t3 in Fig. 9) displayed increasing values because of hot source activation. As can be observed both in Fig. 9(a) and (b) at t1–t3, the thermal gradient was well described by a linear curve with values ranging between 3 °C/cm and 4 °C/cm. It is worth noting that there is a slight difference between $\sigma$ reported in the first test [Fig. 9(a)] and the ones obtained in the second test [Fig. 9(b)]. Indeed, mean $\sigma$ related to the first set range from 0.37 °C to 0.45 °C, while the ones related to the second test are slightly lower (i.e., ranging from 0.11 °C to 0.26 °C). The mentioned differences may be due to the factors influencing the experiments (e.g., the positioning of the FBGs) and the reproducibility of the measuring systems used in the experiments.

Fig. 10(a) and (b) reports the temperature increments as a function of the position recorded by the thermal camera ($\overline{\Delta T}_{IR}(1, j)$) in black dashed line and the ones by the FBG10 (labeled with a blue line) and 1-mm FBGs (i.e., FBG1—orange line, FBG2—yellow line, FBG3—violet line, and FBG4—green line) in each instant (t1–t3) for the first and the second tests, respectively. These plots allow us to compare better the temperature values measured by the two systems (i.e., thermal camera and FBGs). $\Delta T$ values recorded by FBGs of 1 mm are comparable to the ones recorded by the IR images at the same position. Moreover, $\Delta T$ values retrieved from 1 mm FBGs provided thermal gradient information along the 10 mm length. Such analysis could not be performed

TABLE III

$\lambda_B$ VALUES RETRIEVED FOR FBG10 AND FBG1–FBG4 ASSOCIATED WITH $\overline{T}_{IR}$ AT EACH INSTANT (I.E., $t0$–$t3$) FOR THE FIRST AND SECOND BENCH TESTS

| | | $\overline{T}_{IR}$ [°C] | | | | | | | |
|---|---|---|---|---|---|---|---|---|---|
| | | FIRST BENCH TEST | | | | SECOND BENCH TEST | | | |
| | | 26.0 °C | 51.0 °C | 54.1 °C | 55.6 °C | 28.1 °C | 50.0 °C | 53.8 °C | 57.7 °C |
| $\lambda_B$ [nm] | FBG10 | 1533.06 | 1533.30 | 1533.33 | 1533.34 | 1533.06 | 1533.28 | 1533.32 | 1533.34 |
| | FBG1 | 1510.44 | 1510.66 | 1510.70 | 1510.71 | 1510.45 | 1510.66 | 1510.70 | 1510.72 |
| | FBG2 | 1520.38 | 1520.60 | 1520.63 | 1520.66 | 1520.38 | 1520.59 | 1520.63 | 1520.66 |
| | FBG3 | 1530.31 | 1530.57 | 1530.60 | 1530.61 | 1530.31 | 1530.56 | 1530.60 | 1530.62 |
| | FBG4 | 1540.30 | 1540.58 | 1540.60 | 1540.62 | 1540.31 | 1540.56 | 1540.60 | 1540.62 |

TABLE IV

FWHM VALUES OBTAINED FROM FBG10 AND FBG1–FBG4 ASSOCIATED WITH $TG_{IR}$ AT EACH INSTANT (I.E., $t0$–$t3$) FOR THE FIRST AND SECOND BENCH TESTS

| | | $TG_{IR}$[°C] | | | | | | | |
|---|---|---|---|---|---|---|---|---|---|
| | | FIRST BENCH TEST | | | | SECOND BENCH TEST | | | |
| | | 0.3 °C | 4.3 °C | 4.3 °C | 4.3 °C | 0.4 °C | 3.7 °C | 3.8 °C | 4.1 °C |
| FWHM [nm] | FBG10 | 0.59 | 0.59 | 0.59 | 0.59 | 0.60 | 0.59 | 0.59 | 0.59 |
| | FBG1 | 1.96 | 1.96 | 1.96 | 1.96 | 1.95 | 1.94 | 1.95 | 1.95 |
| | FBG2 | 2.06 | 2.05 | 2.06 | 2.05 | 2.04 | 2.03 | 2.03 | 2.03 |
| | FBG3 | 2.10 | 2.10 | 2.11 | 2.11 | 2.14 | 2.12 | 2.12 | 2.12 |
| | FBG4 | 2.20 | 2.20 | 2.21 | 2.20 | 2.20 | 2.20 | 2.20 | 2.20 |

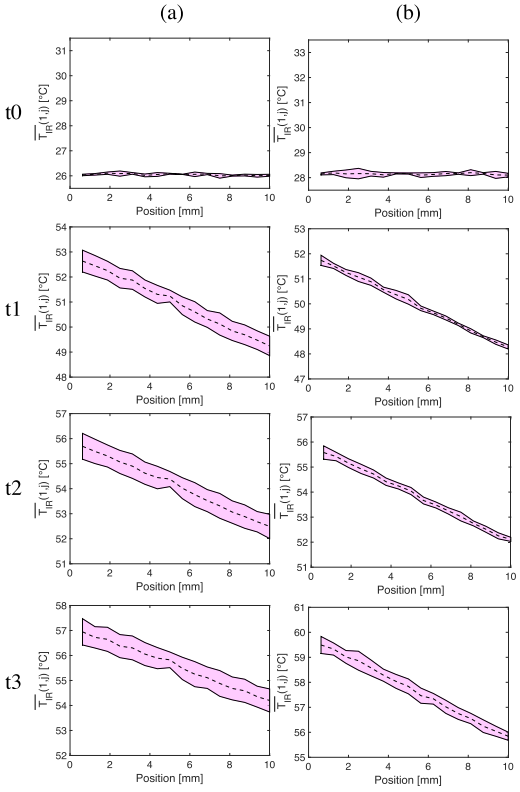


Fig. 9. Average temperature trends—$\overline{T}_{\mathrm{IR}}(1, j)$—(black dotted lines) and standard deviation—$\sigma(1, j)$—(magenta areas) at the four instants (t0–t3) extracted from the IR images for (a) first and (b) second tests, respectively.

using the 10 mm-long FBG, causing the loss of relevant information. However, it is notable that for the second test, temperatures recorded by FBG1 and FBG2 are comparable to each other. This could be due to small variations in FBGs array positioning among the two performed tests.

Table III reports the $\lambda_B$ values against the mean temperature obtained from the IR images (i.e., $\overline{T}_{\mathrm{IR}}$) retrieved in the ROI at each instant for the first and second test, respectively. Data for all FBGs showed that the $\lambda_B$ values increase when the $\overline{T}_{\mathrm{IR}}$ rise for both trials. Table IV shows the FWHM values recorded in correspondence of different thermal gradients (i.e., one for each instance, $TG_{IR}$) extracted from the IR images for both bench tests. In this case, data did not show changes in FWHM values because after hot source activation $TG_{IR}$ values established at the various instants (t1–t3) are comparable to each other and, in any case, low. This occurred in both trials and for all FBGs.

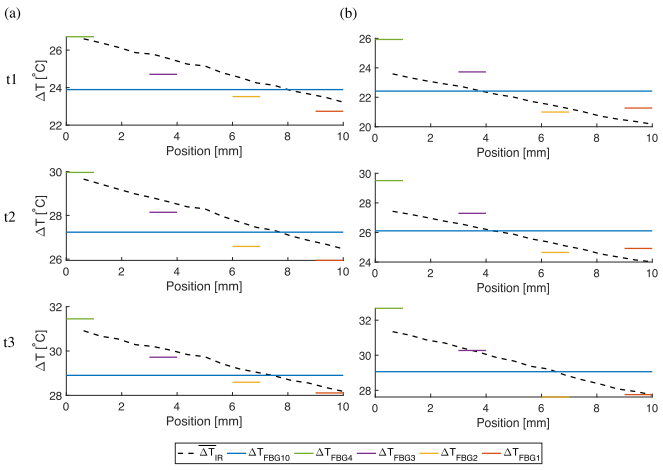


Fig. 10. $\Delta T_{\mathrm{FBG}}$ values recorded from the 1-mm-long FBGs in the 10 mm sensitive length (i.e., $\Delta T_{\mathrm{FBG1}}$ in orange, $\Delta T_{\mathrm{FBG2}}$ in yellow, $\Delta T_{\mathrm{FBG3}}$ in violet, and $\Delta T_{\mathrm{FBG4}}$ in green) compared to the single value retrieved from the 10-mm FBG (i.e., $\Delta T_{\mathrm{FBG10}}$ in blue) and $\overline{\Delta T}_{\mathrm{IR}}(1, j)$ (in black dotted line) from the thermal camera for t1–t3 instants and represented as a function of the position in (a) first and (b) second bench tests.

## IV. INFLUENCE OF TWO BRAGG GRATING LENGTHS ON TEMPERATURE ESTIMATION DURING EX VIVO LA

### A. Experimental Setup of Ex Vivo Trial

To reproduce the presence of relevant and nonlinear thermal gradients as occurs in the real clinical scenario, we performed a LA in freshly excised ex vivo swine liver at fixed power (i.e., 5 W). An Nd:YAG medical laser emitting at 1064 nm commonly employed to treat tumors (Smart 1064 BS, Deka MELA s.r.l., Florence, Italy) was used to induce hyperthermia. This laser uses a quartz optical applicator to guide the energy inside the tissue. To perform the experiment, the upper surface

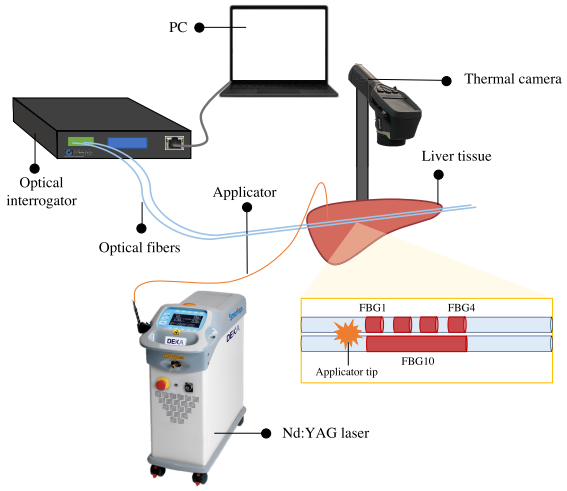


Fig. 11. Experimental setup employed during ex vivo liver LA: ex vivo swine liver, two optical fibers (one housing FBG10 and the other one embedding FBG1–FBG4), an Nd:YAG laser and its applicator to induce hyperthermia, an optical interrogator, a PC, and a thermal camera to collect reference temperature values.

of the ex vivo liver was etched to arrange the fibers. The two above-described optical fibers (i.e., the one equipped with FBG10 and the fiber housing FBG1–FBG4) were relatively positioned as done for bench tests. The applicator was placed on the left end of the array, and the 10-mm sensor (as shown in Fig. 11). The reference instrument and the optical interrogator used for bench tests were employed in this experiment. Thermographic images were acquired at three different time intervals during LA (before, after 26 s, and 36 s from laser source activation), and synchronization with FBG acquisition was performed using a stopwatch. In this case, the $\epsilon$ was set to 0.98, assuming the liver emissivity comparable to the one of human skin. Two needles placed, one on the left and one on the right end of the sensors, were used to easily identify their position inside the organ. Fig. 11 schematically represents the experimental setup employed during LA.

### B. Data Analysis

As done for bench tests, each collected image was initially processed using the thermal camera's software and then imported into MATLAB to obtain the temperature values for the ROI. Thus, it was possible to extract the temperature maps at each instant (i.e., before energy delivery—t0—, after 26 s—t1—, and 36 s—t2—of LA), the mean temperature trend and the related standard deviation (i.e., $\overline{T}_{\mathrm{IR}}(1, j)$ and $\sigma(1, j)$ for t0–t2) in the ROI. After, $\overline{\Delta T_{\mathrm{IR}}}(1, j)$ of the thermal camera was compared with the $\Delta T_{\mathrm{FBG}}$ recorded by 10- and 1-mm FBGs at the same instant. Finally, $\lambda_B$ values and FWHM of the FBGs reflected spectra were related to the $\overline{T_{\mathrm{IR}}}$ and $\mathrm{TG}_{\mathrm{IR}}$, respectively, for further analysis. Please, refer to Section III-B for additional details and a theoretical explanation.

### C. Results

Fig. 12 reports the temperature variations collected by each FBG (i.e., $\Delta T_{\mathrm{FBG}}$) expressed as a function of time acquired during LA. In this case, the highest $\Delta T_{\mathrm{FBG}}$ values were recorded by FBG1, which was the closest to the LA applicator

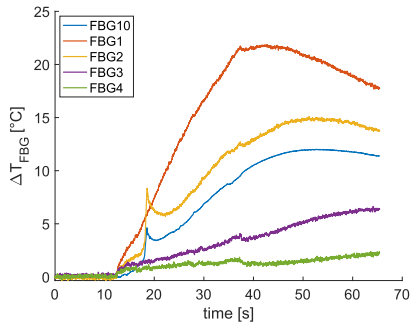


Fig. 12. $\Delta T_{\mathrm{FBG}}$ recorded by the FBGs for the entire acquisition time during the ex vivo LA.

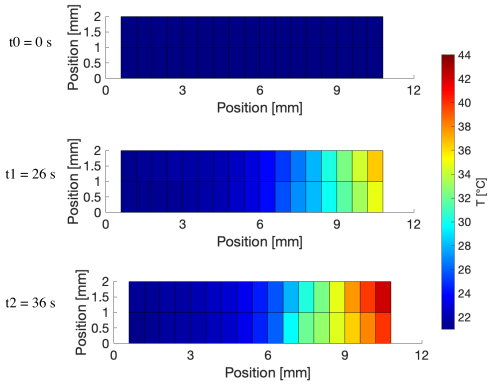


Fig. 13. ROI temperature maps reconstructed from the IR images at specific times (t0-environmental temperature before energy delivery t1 and t2 recorded at 26 and 36 s, respectively, during LA) in ex vivo swine liver.

during the experimental trial. FBG2–FBG4 recorded lower values gradually as they became increasingly distant from the heat source. The maximum $\Delta T_{\mathrm{FBG}}$ value experienced by the FBG1 at the end of discharge (i.e., around 38 s) was around 21 °C. $\Delta T_{\mathrm{FBG}}$ values obtained from FBG10 (i.e., the one long 10 mm) were approximately equal to the average $\Delta T_{\mathrm{FBG}}$ values experienced by the 1-mm FBGs. Compared with bench tests, the thermal gradient occurring was well-marked. Moreover, only FBG2 and FBG10 recorded a sudden $\Delta T$ change around 17 s, which can be probably the result of unintended deformations induced to the sensitive part by the LA applicator.

Fig. 13 shows the ROI temperature maps reconstructed from temperature values extracted by IR images in the area where FBGs were arranged. Before laser energy delivery, an image of the environment temperature was acquired to detect the initial organ temperature. The thermal map related to that instant was reported in Fig. 13 as t0. The maps labeled with t1 and t2 refer to the image acquired at 26 and 36 s during LA with a maximum temperature of around 44 °C (as shown in the t2 map). In this experiment, for both t1 and t2, a marked difference between the cold and hot regions was highlighted, thus revealing a high thermal gradient in the ROI. Fig. 14 refers to the mean temperature trend ($\overline{T}_{\mathrm{IR}}(1, j)$) and the related standard deviation ($\sigma(1, j)$) in the ROI at the three instant times (i.e., t0–t2) calculated from the IR images. Compared with the trend at room temperature (i.e., the one denoted with t0), $\overline{T}_{\mathrm{IR}}(1, j)$ trends at t1 and t2 showed rapid temperature

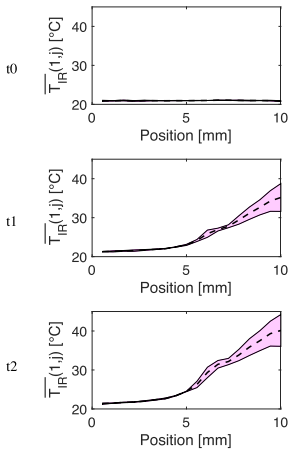


Fig. 14. Average temperature trends—$\overline{T}_{\mathrm{IR}}(1, j)$—(black dotted lines) and standard deviation—$\sigma(1, j)$—(magenta areas) at the three instants (t0–t2) extracted from the IR images.

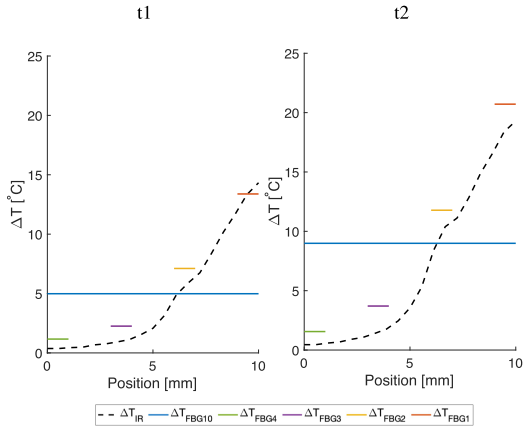


Fig. 15. $\Delta T_{\mathrm{FBG}}$ values recorded from 1-mm-long FBGs in the 10 mm sensitive length (i.e., $\Delta T_{\mathrm{FBG1}}$ in orange, $\Delta T_{\mathrm{FBG2}}$ in yellow, $\Delta T_{\mathrm{FBG3}}$ in violet, and $\Delta T_{\mathrm{FBG4}}$ in green) compared to the single value retrieved from the 10-mm FBG (i.e., $\Delta T_{\mathrm{FBG10}}$ in blue) and $\overline{\Delta T_{\mathrm{IR}}}(1, j)$ (in black dotted line) from the thermal camera for t1, and t2 during ex vivo LA.

increases up to a maximum value in correspondence of the laser applicator position. With respect to previous bench tests, the thermal gradient established was more pronounced, and its value averaged on the whole length of the ROI ranged between 17 °C/cm and 22 °C/cm.

Fig. 15 exhibits a comparison between the average increase recorded by the thermal camera [i.e., $\overline{\Delta T}_{\mathrm{IR}}(1, j)$], reported as black dashed lines, to $\Delta T_{\mathrm{FBG}}$ experienced by the 10-mm FBG (labeled with blue line) and 1-mm FBGs (i.e., FBG1–FBG4 represented with orange, yellow, violet, and green lines, respectively) at t1 and t2. Again, the 1-mm FBGs recorded values comparable to those recorded by the IR images for the same position. As clear evidence, the smaller FBGs followed the $\overline{\Delta T}_{\mathrm{IR}}(1, j)$ trend, thus providing information on the thermal gradient established in the 10 mm, not derived from the more extended sensor.

Tables V and VI report the $\lambda_B$ and FWHM values associated with the $\overline{T}_{\mathrm{IR}}$ and the $\mathrm{TG}_{\mathrm{IR}}$, respectively. Also, in this case, for all FBGs spectra, $\lambda_B$ values increase when the $\overline{T}_{\mathrm{IR}}$ values rise for all the instants. An increase in FWHM values for the 10-mm FBG was evidenced, but the same was not valid for smaller sensors since $\mathrm{TG}_{\mathrm{IR}}$ values acted entirely on the active

TABLE V

$\lambda_B$ VALUES OBTAINED FOR FBG10 AND FBG1–FBG4 ASSOCIATED WITH $\overline{T}_{\mathrm{IR}}$ AT EACH INSTANT (I.E., $t0$–$t2$) FOR EX VIVO LA

| | | $\overline{T}_{IR}$ [°C] | | |
|---|---|---|---|---|
| | | 21.0 °C | 25.8 °C | 28.2 °C |
| $\lambda_B$ [nm] | FBG10 | 1532.99 | 1533.05 | 1533.09 |
| | FBG1 | 1510.38 | 1510.54 | 1510.58 |
| | FBG2 | 1520.31 | 1520.40 | 1520.44 |
| | FBG3 | 1530.26 | 1530.28 | 1530.29 |
| | FBG4 | 1540.26 | 1540.26 | 1540.26 |

TABLE VI

FWHM VALUES OBTAINED FOR FBG10 AND FBG1–FBG4 ASSOCIATED WITH $\mathrm{TG}_{\mathrm{IR}}$ AT EACH INSTANT (I.E., $t0$–$t2$) FOR EX VIVO LA

| | | $TG_{IR}$ [°C] | | |
|---|---|---|---|---|
| | | 0.4 °C | 17.2 °C | 22.7 °C |
| FWHM [nm] | FBG10 | 0.59 | 0.67 | 0.73 |
| | FBG1 | 1.97 | 1.97 | 1.97 |
| | FBG2 | 2.06 | 2.06 | 2.06 |
| | FBG3 | 2.11 | 2.11 | 2.11 |
| | FBG4 | 2.16 | 2.16 | 2.16 |

sensitive length of FBG10. Otherwise, only a small portion of this affected the 1-mm FBGs.

## V. CONCLUSION

In this study, we gathered additional knowledge regarding the impact of two different FBG lengths (i.e., 10 and 1 mm) for temperature measurements in the presence of thermal gradients. To achieve this goal, we carried out both bench tests and ex vivo LA (for a total of three experiments) to replicate, as far as possible, a real clinical scenario. In both cases, we compared the output of a 10-mm-long FBG versus four 1-mm-long FBGs. The edge-to-edge distance (i.e., 2 mm) among the four FBGs allowed covering the sensitive length of the first one to experience the same thermal gradient. For the two bench tests, a linear thermal gradient was imposed by using hot (i.e., cartridge heater) and cold (i.e., a beaker with ice) sources placed on the opposite sides of an ad hoc manufactured aluminum bar. These two tests differed in the set-point temperature imposed on the warmer (i.e., 70 °C and 90 °C). We employed a thermal camera (i.e., FLIR E50, FLIR Systems s.r.l.) as a reference instrument to measure temperatures. The model selected allowed to fulfill the ideal temperature accuracy of 1 °C–2 °C for noninvasive temperature monitoring during hyperthermal ablation therapies [18]. The thermal camera also widely met the requirements in terms of response time, considering that it has a sampling frequency of 60 Hz (16.7 ms) and the sensor embedded in this camera has a time constant of about 10 ms. This solution allowed us to gain comprehensive temperature knowledge experienced by the FBGs and to reconstruct the temperature distribution in the ROI (i.e., those related to the FBG positioning). Thus, we overcome the limitations of the interesting experiments reported in [26]. Indeed, in this previous study, two thermocouples were used as reference temperature instruments positioned at the right and the left end of a 10-mm FBG. Although this approach allows estimating the thermal gradient between the two extremities of the FBG, it precludes deriving information such as the temperature distribution and the average temperature trend ($\overline{\Delta T}_{\mathrm{IR}}(1, j)$) within the ROI. Furthermore, in [26], authors compared the output of the

10-mm sensor with those of three FBG 1 mm long and 2 mm spaced (for a total of 7 mm); thus, there was not a perfect match between the length covered by the three 1-mm-long FBGs and the one covered by the 10-mm-long FBG. The experimental results reported in this study showed a linear thermal gradient ranging between 3 °C/cm and 4 °C/cm, for the first and second trials, respectively. The comparison of temperatures measured by the two different systems (i.e., thermal camera and FBGs) revealed similar values obtained from the 1-mm-long sensors (i.e., $\Delta T_{\mathrm{FBG1}}$, $\Delta T_{\mathrm{FBG2}}$, $\Delta T_{\mathrm{FBG3}}$, and $\Delta T_{\mathrm{FBG4}}$) to those from IR images [i.e., $\overline{\Delta T}_{\mathrm{IR}}(1, j)$] for the same position, highlighting the ability of the shorter sensors to reconstruct the established thermal gradient trend. Otherwise, the 10-mm-long FBG showed values (i.e., $\Delta T_{\mathrm{FBG10}}$) comparable to the average of the values obtained with 1-mm FBGs, thus hiding the real temperature trend established along its length. As evidenced in Fig. 10(a) and (b), the difference between the $\Delta T$ recorded by FBG10 and the one recorded by FBG4 experienced the maximum variation ranging between 3 °C and 4 °C for the two trials. So, in a real scenario, the use of an FBG with a longer length results in measurement errors regarding the temperature reached inside the tissue that could lead to a poor approximation of the thermal damage inflicted. As expected, spectral response analysis showed an increase in $\lambda_B$ values of each FBG (i.e., FBG10 and FBG1–FBG4) in correspondence with a rise in the mean temperature (i.e., $\overline{T}_{\mathrm{IR}}$) in the ROI, for both cases. Predictably, the maximum shift in $\lambda_B$ was recorded between t0 and t1 (i.e., before and after 186 or 188 s the activation of hot and cold sources) with a maximum of 0.26 nm. For the case of close acquisition times (i.e., between t1 and t2 and t2 and t3) involving smaller $\overline{T}_{\mathrm{IR}}$ variations, no significant $\lambda_B$ changes (up to 0.04 nm) were recorded. Data did not evidence substantial changes in FWHM values for all FBGs in response to the change in thermal gradient reconstructed from IR images (i.e., $\mathrm{TG_{IR}}$), explainable because of the small $\mathrm{TG_{IR}}$ established in both tests (up to 4 °C/cm). Aiming to reproduce a marked thermal gradient as it occurs in clinical scenarios, we subjected an ex vivo swine liver to LA fixing a power equal to 5 W. In this case, the two optical fibers were arranged on the tissue, previously etched to create a surface cavity, and an Nd:YAG laser worked to induce a significant temperature variation along the gratings. A similar investigation was also carried out by [26] and [27]. However, in [26], the influence of FBG length (10 versus 1 mm) under substantial gradient was assessed only in terms of $\Delta\lambda_B$ and without any kind of reference instrument. Instead, in [27], ex vivo LA was mimicked by an agar phantom heated with a linear resistor and therefore differed from real conditions both in terms of temperature distribution induced and tissue properties. In their study, the output of an FBG 15 mm long was compared with the ones of three FBGs 1 mm each and with a distance edge-to-edge of 4 mm, employing four thermocouples to reconstruct the temperature profile from the resistor to one of the phantom edges. These reference temperature sensors did not allow for a complete reconstruction of the temperature distribution around the treated area as the one obtained from the thermal camera in our study (as shown in Fig. 13). For this scenario, we obtained a much stronger gradient than in bench tests, characterized by a nonlinear behavior and ranging between 17 °C/cm and 22 °C/cm (Fig. 14). As found for the previous case and evidenced in Fig. 15, the $\Delta T_{\mathrm{FBG1}}$, $\Delta T_{\mathrm{FBG2}}$, $\Delta T_{\mathrm{FBG3}}$, and $\Delta T_{\mathrm{FBG4}}$ are comparable to the $\overline{\Delta T}_{\mathrm{IR}}(1, j)$ for the same position in both time instants (i.e., t1 and t2) at which IR images were acquired while the single $\Delta T_{\mathrm{FBG10}}$ value only provided the average temperature along the sensitive length. Moreover, differently from bench tests, in this case, we obtained more pronounced differences between the FBG10 and the FBG1 recording the highest temperature (i.e., around 8 °C and 11 °C in the two acquisition times). This result points out that in a scenario similar to the real one, the error committed by the longer sensor is even higher and, therefore, not tolerable, as thermal gradients occurring are considerably stronger. As for the results obtained in a controlled environment, changes in $\lambda_B$ values resulted in a response to the temperature increment for all the FBGs except the FBG4, which did not record any change for the entire duration of the test. Contrary to the bench test results, we found evident changes in FWHM values (up to 0.14 nm of variation) for FBG10 when the gradient was established, not observable in 1-mm-long FBGs. This is reasonable because only the longer FBG was exposed to the whole thermal gradient.

In conclusion, our findings highlight the higher suitability of FBGs array with respect to long FBGs in TAT applications, especially in the case of relevant thermal gradients, since their use might lead to unacceptable measurement errors, implying inaccurate assumptions about the procedure outcome. However, a limited number of trials were conducted, and future tests will be devoted to increasing the sample size for corroborating the results.

## REFERENCES


[1] J. K. Sahota, N. Gupta, and D. Dhawan, "Fiber Bragg grating sensors for monitoring of physical parameters: A comprehensive review," *Opt. Eng.*, vol. 59, no. 6, 2020, Art. no. 060901.

[2] M. Mishra and P. K. Sahu, "Fiber Bragg gratings in healthcare applications: A review," *IETE Tech. Rev.*, vol. 40, no. 2, pp. 1–18, 2022.

[3] D. Lo Presti et al., "Fiber Bragg gratings for medical applications and future challenges: A review," *IEEE Access*, vol. 8, pp. 156863–156888, 2020.

[4] V. Mishra, N. Singh, U. Tiwari, and P. Kapur, "Fiber grating sensors in medicine: Current and emerging applications," *Sens. Actuators A, Phys.*, vol. 167, no. 2, pp. 279–290, Jun. 2011.

[5] G. Alvarez-Botero, F. E. Baron, C. C. Cano, O. Sosa, and M. Varon, "Optical sensing using fiber Bragg gratings: Fundamentals and applications," *IEEE Instrum. Meas. Mag.*, vol. 20, no. 2, pp. 33–38, Apr. 2017.

[6] S. Korganbayev et al., "PID controlling approach based on FBG array measurements for laser ablation of pancreatic tissues," *IEEE Trans. Instrum. Meas.*, vol. 70, pp. 1–9, 2021.

[7] G. Palumbo et al., "Temperature profile of ex-vivo organs during radio frequency thermal ablation by fiber Bragg gratings," *J. Biomed. Opt.*, vol. 21, no. 11, Nov. 2016, Art. no. 117003.

[8] F. De Tommasi et al., "Fiber Bragg grating sensors for temperature monitoring during thermal ablation procedure: Experimental assessment of artefact caused by respiratory movements," *IEEE Sensors J.*, vol. 21, no. 12, pp. 13342–13349, Jun. 2021.

[9] H. H. Abd Raziff et al., "A temperature-controlled laser hot needle with grating sensor for liver tissue tract ablation," *IEEE Trans. Instrum. Meas.*, vol. 69, no. 9, pp. 7119–7124, Sep. 2020.

[10] N. T. Pham, S. L. Lee, S. Park, Y. W. Lee, and H. W. Kang, "Real-time temperature monitoring with fiber Bragg grating sensor during diffuser-assisted laser-induced interstitial thermotherapy," *J. Biomed. Opt.*, vol. 22, no. 4, Apr. 2017, Art. no. 045008.

[11] I. F. Saxena, K. Hui, and M. Astrahan, "Polymer coated fiber Bragg grating thermometry for microwave hyperthermia," *Med. Phys.*, vol. 37, no. 9, pp. 4615–4619, Aug. 2010.
[12] K. F. Chu and D. E. Dupuy, "Thermal ablation of tumours: Biological mechanisms and advances in therapy," *Nature Rev. Cancer*, vol. 14, no. 3, pp. 199–208, Mar. 2014.
[13] S. N. Goldberg, G. S. Gazelle, and P. R. Mueller, "Thermal ablation therapy for focal malignancy: A unified approach to underlying principles, techniques, and diagnostic imaging guidance," *Amer. J. Roentgenol.*, vol. 174, no. 2, pp. 323–331, 2000.
[14] J. A. Pearce, "Models for thermal damage in tissues: Processes and applications," *Crit. Reviews Biomed. Eng.*, vol. 38, no. 1, pp. 1–20, 2010.
[15] M. H. H. Tehrani, M. Soltani, F. M. Kashkooli, and K. Raahemifar, "Use of microwave ablation for thermal treatment of solid tumors with different shapes and sizes—A computational approach," *PLoS ONE*, vol. 15, no. 6, Jun. 2020, Art. no. e0233219.
[16] E. De Vita et al., "Investigation of the heat sink effect during microwave ablation in hepatic tissue: Experimental and numerical analysis," *IEEE Sensors J.*, vol. 21, no. 20, pp. 22743–22751, Oct. 2021.
[17] H.-W. Huang, "Influence of blood vessel on the thermal lesion formation during radiofrequency ablation for liver tumors," *Med. Phys.*, vol. 40, no. 7, Jun. 2013, Art. no. 073303.
[18] L. Frich, "Non-invasive thermometry for monitoring hepatic radiofrequency ablation," *Minimally Invasive Therapy Allied Technol.*, vol. 15, no. 1, pp. 18–25, Jan. 2006.
[19] P. Saccomandi, E. Schena, and S. Silvestri, "Techniques for temperature monitoring during laser-induced thermotherapy: An overview," *Int. J. Hyperthermia*, vol. 29, no. 7, pp. 609–619, Nov. 2013.
[20] A. J. Welch et al., *Optical-Thermal Response of Laser-Irradiated Tissue*, vol. 2. Cham, Switzerland: Springer, 2011.
[21] N. Chen et al., "In vivo experiments of laser thermotherapy on liver tissue with FBG temperature distribution sensor," in *Proc. SPIE*, vol. 8376, 2012, pp. 68–73.
[22] E. De Vita et al., "Multipoint temperature monitoring of microwave thermal ablation in bones through fiber Bragg grating sensor arrays," *Sensors*, vol. 20, no. 11, p. 3200, Jun. 2020.
[23] Y. Ding, N. Chen, Z. Chen, F. Pang, X. Zeng, and T. Wang, "Dynamic temperature monitoring and control with fully distributed fiber Bragg grating sensor," in *Proc. SPIE*, vol. 7845, 2010, pp. 45–50.
[24] Y.-J. Rao, D. J. Webb, D. A. Jackson, L. Zhang, and I. Bennion, "In-fiber Bragg-grating temperature sensor system for medical applications," *J. Lightw. Technol.*, vol. 15, no. 5, pp. 779–785, May 1997.
[25] A. Othonos, K. Kalli, D. Pureur, and A. Mugnier, "Fibre Bragg gratings," in *Wavelength Filters in Fibre Optics*. Cham, Switzerland: Springer, 2006, pp. 189–269.
[26] S. Pangaro et al., "Influence of fiber Bragg grating length on temperature measurements in laser-irradiated organs," in *Proc. IEEE Int. Symp. Med. Meas. Appl. (MeMeA)*, May 2016, pp. 1–6.
[27] R. Gassino, G. Perrone, and A. Vallan, "Temperature monitoring with fiber Bragg grating sensors in nonuniform conditions," *IEEE Trans. Instrum. Meas.*, vol. 69, no. 4, pp. 1336–1343, Apr. 2020.
[28] T. Erdogan, "Fiber grating spectra," *J. Lightw. Technol.*, vol. 15, no. 8, pp. 1277–1294, Aug. 1997.
[29] Y.-J. Rao, "Fiber Bragg grating sensors: Principles and applications," in *Optical Fiber Sensor Technology*. Cham, Switzerland: Springer, 1998, pp. 355–379.
[30] D. A. Hackney, K. J. Peters, R. J. Black, J. M. Costa, and B. Moslehi, "Fiber Bragg gratings as transient thermal gradient sensors," *Opt. Eng.*, vol. 55, no. 11, Nov. 2016, Art. no. 114102.
[31] A. P. D. Varalda et al., "Assessment of a linearly chirped fiber Bragg grating sensor under linear and non-linear temperature gradient," in *Proc. IEEE Int. Instrum. Meas. Technol. Conf. (IMTC)*, May 2017, pp. 1–6.
[32] P. Saccomandi et al., "Linearly chirped fiber Bragg grating response to thermal gradient: From bench tests to the real-time assessment during in vivo laser ablations of biological tissue," *J. Biomed. Opt.*, vol. 22, no. 9, 2017, Art. no. 097002.
[33] TO Components. (2023). *Technica Optical Components Customized FBG Sensor*. [Online]. Available: https://technicasa.com/wp-content/uploads/2017/01/T10-Customized-FBG-Sensor-1.pdf
[34] (2023). *Technica Optical Components FBG Sensing Array*. [Online]. Available: https://technicasa.com/wp-content/uploads/2017/01/T100-FBG-Sensing-Array-.pdf
[35] FLIR. *Technical Data*. [Online]. Available: http://docs.rs-online.com/ca3e/0900766b81371810.pdf

**Francesca De Tommasi** (Student Member, IEEE) received the M.Sc. degree (cum laude) in biomedical engineering from Università Campus Bio-Medico di Roma (UCBM), Rome, Italy, in 2020, where she is currently pursuing the Ph.D. degree in bioengineering.

Her research interests focus on the development of fiber Bragg grating (FBG)-based measurement systems for biomedical applications.

**Livio D'Alvia** (Member, IEEE) received the joint Ph.D. degree in industrial and management engineering from Roma Tre University, Rome, Italy, and the University of Rome La Sapienza, Rome, in 2018.

He is currently a Research Fellow of industrial and mechanical measurements at the University of Rome La Sapienza. His current research spreads from the measurements for industrial and biomedical applications and to the measurements for cultural heritage.

**Carlo Massaroni** (Senior Member, IEEE) received the Ph.D. degree in biomedical engineering from the Università Campus Bio-Medico di Roma, Selcetta, Italy, in 2017.

He is currently an Assistant Professor of measurements at Università Campus Bio-Medico di Roma (UCBM), Rome, Italy. His research interests include the design, development, and testing of wearable devices and unobtrusive measuring systems for medical applications.

**Daniela Lo Presti** (Member, IEEE) received the Ph.D. degree in bioengineering from the Università Campus Bio-Medico di Roma, Selcetta, Italy, in 2020.

She is currently Assistant Professor at Università Campus Bio-Medico di Roma (UCBM), Rome, Italy. Her research interests focus on the design, fabrication, and assessment of fiber Bragg gratings (FBGs)-based tools and wearables for medical and biomedical applications.

**Massimiliano Carassiti** is currently an Anesthesiologist and an Associate Professor in anesthesia at Università Campus Bio-Medico di Roma (UCBM), Rome, Italy. His main research interests include anesthesiology, intensive care medicine, pain medicine and management, and the development of smart systems to support physicians during epidural procedures.

**Zaccaria Del Prete** (Member, IEEE) is a Full Professor of industrial and biomedical measurements with the Department of Mechanical and Aerospace Engineering, Sapienza University of Rome, Rome, Italy. His research interests in the biomedical field spread from experimental analysis of mechanoreceptor neurons coding mechanism and the mechanical properties of viscoelastic biological soft tissue, in vitro analysis of the flow stream through the artificial cardiac valve by particle image velocimetry, and in vitro analysis of transgenic muscle fiber and tendon biomechanical properties.

**Emiliano Schena** (Senior Member, IEEE) received the Ph.D. degree from the Università Campus Bio-Medico di Roma, Selcetta, Italy, in 2007.

He is a Full Professor of measurements with Università Campus Bio-Medico di Roma (UCBM), Rome, Italy. His main research interests include the design and assessment of wearable systems for vital signs monitoring, applications of fiber optic sensors in medicine, and thermal ablation for cancer removal.

**Eduardo Palermo** (Member, IEEE) received the Ph.D. degree in 2014.

He is currently an Assistant Professor with the Department of Mechanical and Aerospace Engineering, Sapienza University of Rome, Rome, Italy. His main research interests include the design, implementation, and validation of new technologies, wearable inertial sensors, machine learning algorithms, mechatronics, human–computer interactions, and bio-signal processing.

Open Access funding provided by 'Università "Campus Bio-Medico" di Roma' within the CRUI CARE Agreement